Modeling and Control of an Insect-Scale Legged Microrobot

Final Design Report

Jack Long

Cornell University
School of Mechanical and Aerospace Engineering
Helbling Research Laboratory

March 4, 2026

Contents

Executive Summary

Abstract

Autonomy remains a challenge in insect-scale robot platforms due to the size, weight, and power requirements of onboard sensing and control electronics. In this work, we present a strategy for hardware implementation of onboard sensing and control of the Cornell MicroTerrestrial (COMT) robot, a 1.5-g electromagnetically-actuated insect-scale quadruped. We integrate off-the-shelf inertial and time-of-flight sensor packages with a microcontroller, power electronics, and DC motor drivers, enabling position and orientation control. The complete system is realized on a custom lightweight printed circuit board (PCB), expanding untethered capabilities compared to previous iterations.

1 Desired Functions

The COMT control system, defined as the electronics and software of the COMT robot, must include:

- **Feedback Control**: Application of a control signal to the robot's actuators based on current and target state.
- **Control Authority**: Control of the robot to reliably reach a target state in a controlled environment.
- **Autonomous Operation**: Realization of the above requirements without external input.
- **Architecture Flexibility**: Tunability of the control system for a wide range of possible transmission geometries.

2 Constraints

COMT has strict size, weight, and power (SWaP) requirements, which are motivated primarily by the system's requirement to (a) carry its own energy storage and (b) produce enough force to propel the combined weight of its chassis, actuators, battery, and electronics. The 1.5-g robot consumes approximately 1.1 W at maximum power. For successful operation, we require that:

- The physical electronics must conform to the existing robot chassis and minimize mass to minimize the robot's cost of transport.
- The sensing and control electronics must draw very little power relative to the actuators to maximize runtime.
- The control loop must compute and be able to apply control input no slower than the actuation frequency of the robot.

3 Quantitative Performance Objectives

- System current draw < 300 mA during normal gait
- Printed circuit board (PCB) mass < 500 mg
- Peak control loop frequency twice as fast as the drive frequency f_d.
- PCB width < 19 mm to accommodate chassis manufacturing constraints.

4 Alternative Design Concepts

Control Strategy:

- Frequency-based control, whereby legs on either side of the robot are actuated at different frequencies, was considered based on a proposal in [1], but tested and found to lack control authority on its own in COMT.
- Phase-based control, where the timing between leg actuations controls the turning force of the robot, was tested in conjunction with variable-frequency gaits. However, this strategy exhibited unpredictable dynamics in our desired operating regions.

Electronics:

- A PCB unifying power and control electronics on one face of COMT was considered, but the additional footprint required to actuate each degree of freedom (DOF) individually was prohibitively large. Additionally, maintaining proper ground return paths, one of the issues identified in the previous PCB, was much more difficult in a single PCB laminate.

5 Selection Criteria

We selected the control strategy using experimental analysis and comparing different strategies proposed in literature [2] [3]. Because so many parameters were involved in the design of the PCB, a weighted decision matrix was used to determine the best overall structure for the design. Individual scores were determined both by engineering fundamentals, like safety factor of each design under the flexural stresses associated with worst-case system operation, and empirical observations, like observed crosstalk between actuator signal and microcontroller input voltage in the previous PCB.

Table 1: Decision Matrix for PCB Architecture Selection

Criterion	**Weight (%)**	**Unified (Weighted)**	**Split (Weighted)**
Footprint / routing area per DOF	25	50	125
Ground return path quality & loop control	20	40	80
Electrical separation / noise isolation	20	40	100
Mechanical robustness of interconnects	15	60	30
Manufacturability / assembly complexity	10	40	30
Scalability / future modifications per DOF	10	30	40
Total		**260**	**405**

6 Industry Standards

All code written is in accordance with the C-99 specification, followed by the MCUXpresso IDE default C compiler. This specification restricts the operators and datatypes available compared to newer standards, but is well-documented and stable. Multiple digital communication protocols, primarily Inter-Integrated Circuit (I2C) and Serial Wire Debug (SWD), informed the layout and component selection of the PCB. Additional PCB design considerations were derived from the Global Electronics Association's IPC-2221A [4].

7 Coursework Application

- **ENGRD/ECE 2300: Digital Logic and Computer Organization**. Understanding of microprocessor operations gained from building an FPGA-based single-cycle microprocessor allowed me to select performant data structures and minimize computational overhead of sensor peripherals with interrupts.

- **ENGRD/ECE 2100: Introduction to Circuits for Electrical and Computer Engineers**. EE fundamentals and prototyping strategies learned through ECE 2100 lab allowed me to size and place PCB elements according to their operating conditions, and to create representative prototypes to evaluate subsystems.
- **MAE 3260: System Dynamics**. A working knowledge of linear systems allowed me to evaluate the dynamic modeling of robots similar to COMT in literature and apply relevant concepts to COMT. The study of mechanical resonance in the MAE 3260 lab component facilitated my understanding of COMT's open-loop actuation strategy and transmission model.
- **MAE 3240: Heat Transfer**. Drawing high current in a small footprint requires serious consideration of thermal losses. Understanding of heat transfer mechanisms from MAE 3240 helped me to with thermal modeling of the voice coil actuators.
- **MAE 4870: Feedback Control Systems**. The selection and tuning of closed-loop control strategies learned in MAE 4870 inspired me to build COMT's control strategy in multiple nested loops instead of a monolithic loop for ease of heuristic tuning.
- **MAE 4190: Fast Robots**. Fast Robots taught me how to navigate the unique implementation constraints of autonomous systems which must apply control inputs faster than their sensors can sample, as well as work with the specific sensor systems employed on COMT in a computationally-efficient way.

8 Design Evaluation and Existing Solutions

The following objectives were evaluated:

- **Control Authority:** Control authority of the entire COMT system was unable to be verified due to time constraints in actuator manufacturing. However, the variable displacement of actuators necessary for control authority was demonstrated for an individual leg via pulse width modulation (PWM).
- **Feedback Control:** Raw data from the onboard sensor suite was filtered and compared to a target state, then mapped to a control input signal to the motor drivers (DRV8833, Texas Instruments). Resulting motor driver outputs successfully tracked state error.
- **Untethered Operation:** Untethered control remains untested, but capabilities of the improved onboard control PCB enable individual actuation of each DOF.
- **Flexibility:** Variable displacement via current control was achieved for one leg configuration with minimal ripple current losses.

At the insect scale, the most sophisticated crawling robot is the Harvard Ambulatory MicroRobot (HAMR) [5], a piezoelectrically-actuated quadruped designed at the Harvard Microrobotics Laboratory. HAMR achieves greater maneuverability and power efficiency than COMT at the cost of greater manufacturing complexity. HAMR achieves onboard trajectory control using an inertial measurement unit (IMU) and optical mouse sensor [6], while COMT uses an IMU and time-of-flight (TOF) sensor. The TOF sensor, while more reliant on the robot's environment for position estimation, is significantly smaller and lighter than off-the-shelf optical mouse sensors. Additionally, the TOF sensor enables future onboard localization and mapping, both of which are necessary for any real-world operating conditions. Electromagnetically-actuated systems like VelociROACH [7] and BHMBot [8] also demonstrate signficantly greater straight-line speeds (27 BL/s and 29.2 BL/s, respectively.

9 Impact

The COMT system is designed with low-footprint, autonomous monitoring in mind, especially of sensitive ecosystems vulnerable to human disturbance or space-constrained environments dangerous or inaccessible to humans (such as aircraft engines). Environmental monitoring of sensitive ecosystems would allow for better examination of human impact on the natural world, potentially informing sustainability initiatives seeking to characterize and limit human interference in the natural environment. Inspection of space-constrained hazardous environments with autonomous microrobots like COMT directly improves human safety, especially in high-risk fields like aircraft or nuclear maintenance. Additionally, the similarity in form of legged microrobots to insects could make make them an approachable gateway for children into the world of robotics, making COMT not only a useful platform for industry, but also for STEM educators.

10 Design Format

The control system encompasses the electronic hardware mounted on the robot chassis, and the software running on these electronics. The hardware takes the form of a flexible PCB, which connects commercial, off-the-shelf (COTS) integrated circuits (IC), including a microcontroller, sensor suite, and power system. The software running on the microcontroller is written in the C programming language, and implements a custom sensing and control strategy informed by open-source libraries.

11 Roles

Julie Villamil, an ECE Ph.D. candidate, is the primary contributor to the COMT system and designed the chassis, legs, and actuators of the robot. Julie additionally developed and ran most of the simulations referenced in the report. I designed the control system, electronic hardware, and software implementation of our sensing and control strategy.

Final Report

1 Introduction

Microrobotic platforms have traditionally required highly specialized fabrication methods and actuation schemes for locomotion. These constraints have limited their practicality both for real-world deployment and for use as experimental tools in robotics, sensing, and multi-agent research. The Cornell MicroTerrestrial (COMT) robot, a quadrupedal microrobot developed by Professor Helbling's research group, is intended to address this gap by providing a stable, modular, and fully autonomous platform based on PC-MEMS technology [9]. Its design targets several research objectives: the integration and testing of small-scale sensor systems, monolithic fabrication methods, and investigation of communication and control strategies for microrobot collectives. To date, the group has demonstrated open-loop locomotion of COMT. This work focuses on increasing control authority and power efficiency of the robot towards untethered, closed-loop control.

COMT uses voice coil actuators (VCAs) to eliminate the high voltage requirements and low displacements of similar microrobotic actuation strategies, such as piezoelectric benders. [5]. VCAs generate force through the Lorentz interaction between a current-driven coil and a fixed magnetic field, enabling millimeter-scale displacements and (~ 10 mN) of force at supply voltages below 5 V. This makes them well-suited for legged microrobots, where their high stroke at low voltage removes the need for inefficient boost converters and permits mechanically simple transmissions capable of large stride lengths.

2 Open-Loop Control and Performance

COMT has eight total degrees of freedom (DOFs): One 'lift' and one 'swing' per leg, that are translated into leg motion via two planar four-bar linkages (see Figure 1). Phasing of these DOFs is a well-established method for stability and control in quadrupeds at all scales [2, 10], and is defined in terms of the stride frequency f_d, inter-leg phase ϕ_g and intra-leg phase ϕ_p, according to the following definitions:

- *Inter-leg phasing* controls the relative footfall timing between front, rear, left, and right legs, allowing us to specify canonical quadruped gaits (e.g., trot, pronk, pace, bound) [11]. For example,

  $$\{\phi_{g,\mathrm{FL}}, \phi_{g,\mathrm{FR}}, \phi_{g,\mathrm{RL}}, \phi_{g,\mathrm{RR}}\} = \{0^\circ, 180^\circ, 180^\circ, 0^\circ\}$$

  describes a trot.

- *Intra-leg phasing* sets the local timing between lift and swing DOFs, controlling the shape of leg tip trajectory. $\phi_p = 90^\circ$ produces a circular trajectory when both DOFs are actuated sinusoidally.

The motion of each DOF can then be described fully with f_d and the net phase of each actuator

$$\phi_i = \phi_g + \phi_p. \tag{1}$$

We evaluated different control schemes within this framework to maximize standard performance metrics in terrestrial microrobots [11] while maintaining power efficiency for autonomous operation.

2.1 Control Strategy

We first tested the phase control scheme presented in [2], which introduces an orientation phase ϕ_t. A turn is generated by adding or subtracting ϕ_t to ϕ_i in swing DOFs, depending on desired direction. During these experiments, actuators in both lift and swing DOFs varied greatly in leg-to-leg displacement, indicating that significant open-loop tuning was necessary for establishing control authority. We observed that varying f_d around the performance peaks observed in Section 2.7 produced consistent and monotonic changes in open-loop trajectory to this end. For example, decreasing frequency below the peak-velocity condition reduced asymmetry in a left-side-weak robot, and vice versa, although the underlying dynamics responsible

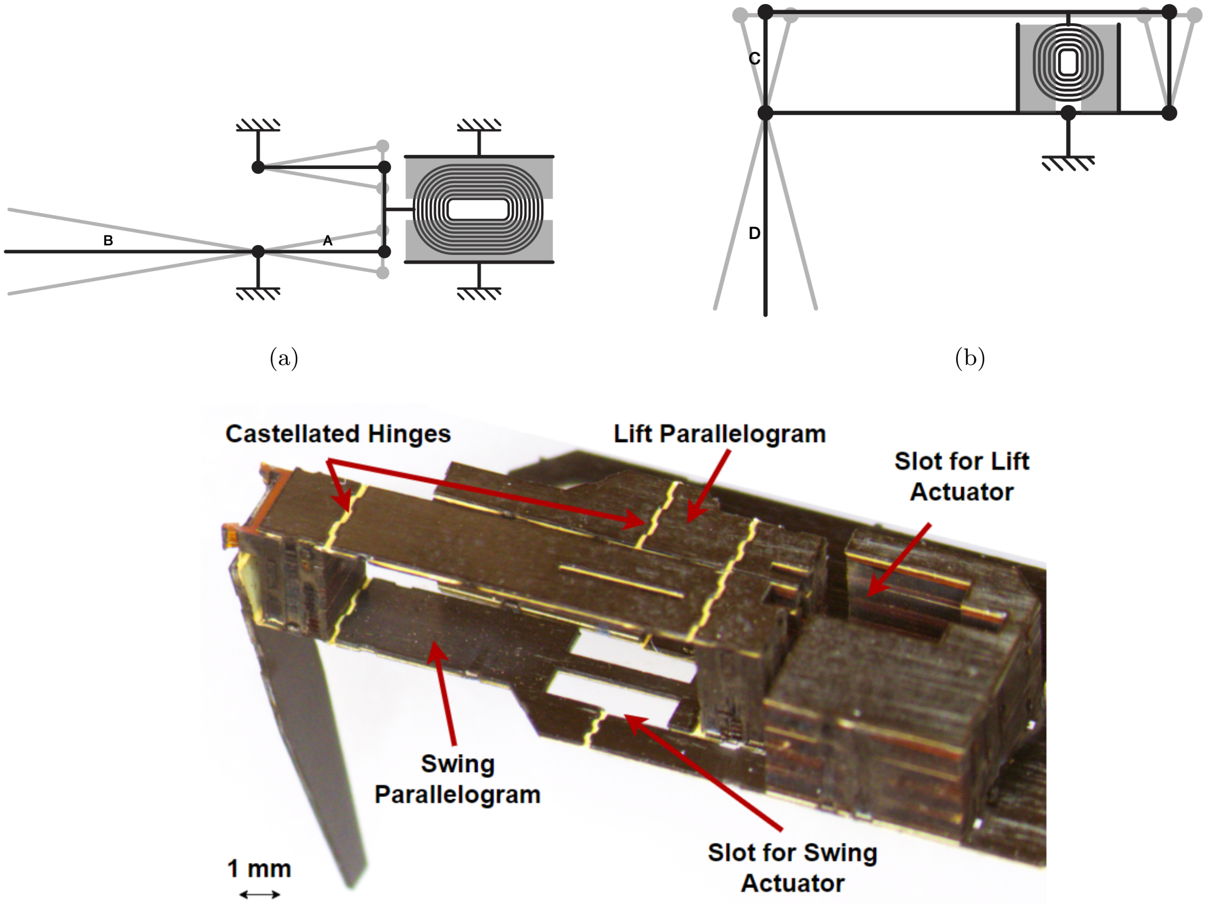

(a)

(b)

(c)

Figure 1: Schematic and implementation of series lift and swing mechanisms. (a) The lift coil drives a parallelogram linkage vertically, with motion amplified by the transmission at ratio A:B. (b) The swing coil drives a parallelogram linkage laterally, with motion amplified at ratio C:D. (c) Lift and swing linkages are assembled in series.

for this behavior were unclear. Additionally, the map from ϕ_p and ϕ_t to observed trajectories was strongly non-monotonic. Small changes in each produced disproportionate and inconsistent yaw rates, rendering closed-loop tuning under this control impractical for reliable operation.

Frequency-based control, in which legs on either side of the robot are actuated at different drive frequencies, was also considered based on a proposal in [2], but was found to lack reliable turning authority when applied to COMT. Because the frequency-based scheme does not enforce a phase between left and right actuation, the inter-leg footfall timing varied continuously. As a result, the net effect of actuator inputs on the robot dynamics was unpredictable. It is likely that the variable timing of footfall impulses excited undesirable resonances in the chassis and legs of the robot, producing leg-tip motions that disrupted repeatable leg trajectories and reliable system performance.

More broadly, both previously-tested frequency- and phase-based strategies required operation away from mechanically advantageous leg or body resonance modes. Detrimental effects of this operation are evident both in the leg displacement experiments presented in Section 2.6 and in open-loop peak straight-line speed measurements of the robot in Section 2.7. Any control authority gained through deliberate frequency detuning is thus outweighed by performance losses and reduced reliability, making off-resonance operation unsuitable as a long-term closed-loop control strategy.

2.2 Current-Controlled Differential Drive

To avoid issues posed by the above strategies, We employ a control scheme which varies the current I_{eff} through each actuator via pulse-width modulation (PWM), an established method for current control in larger electromagnetic actuators [12]. We hypothesize that current control will provide greater tuning capability in tandem with the phase-based methods explored in the previous section.

PWM drives the planar voice-coil actuators by rapidly switching the coil voltage between 0 V and the supply V_{in}, controlling force through the duty cycle rather than an analog current command. The inductive dynamics of the coil low-pass the switching waveform, so the actuator experiences an effective current proportional to the duty cycle D:

$$I_{\text{eff}} = D\frac{V_{\text{in}}}{R} \tag{2}$$

This allows for control of Lorentz force, which scales with current, without the negative footprint and power efficiency impacts of switching regulators. By controlling this force within each actuator, we can produce varying leg tip trajectories; varying the cycle-averaged displacement of left and right sides of the robot induces a turn.

The carrier frequency of the PWM signal is a necessary consideration for both power efficiency and control precision. Our low drive frequency (in the tens of Hz) means that traditional PWM frequencies in the kHz range are more than adequate for a smooth observed trajectory. However, the actuator coils' low inductance relative to their DC resistance mean that power losses due to ripple current at a particular PWM frequency must also be considered [13] .

While Lorentz force production scales with average current, power dissipated in the actuator scales with root-mean-squared (RMS) current, a metric dependent on the magnitude of high-frequency ripple experienced by the actuator coil. This magnitude is set primarily by the ratio L/R and the PWM frequency. For an RL coil, the electrical time constant is $\tau_e = L/R$. If the PWM period T is large compared to τ_e, the inductor current changes substantially within each switching cycle, producing a large exponential ripple.

We quantified the effect of ripple current losses by measuring current draw at various duty cycles in the lift ($R = 60.1\ \Omega$, $L \approx 350\text{mH}$) and swing ($R = 40.3\ \Omega$, $L \approx 270\text{mH}$) VCAs. All tests were conducted at $f_{\text{PWM}} = 24$ kHz to attempt to reproduce high ripple current at the nominal battery voltage of 3.7 V, while still remaining out of the human-audible frequency range. We verified the expected duty–current linearity, as shown in Figure 2, and observed little deviation ($\sim 5\%$) from the ideal duty–current curve. We concluded that the combination of additional low-passing dynamics in the motor driver and mechanical constraints preventing the VCA from displacing (i.e., doing work) at such high frequencies mitigated ripple current losses. To reduce potential switching losses introduced by higher-frequency PWM, we continued operating at 24 kHz for the remainder of experiments.

2.3 VCA Characterization

We characterized the actuators used in subsequent sections with current-displacement data collected from actuators installed in the leg. Video of the actuated transmission was taken on a high-speed camera

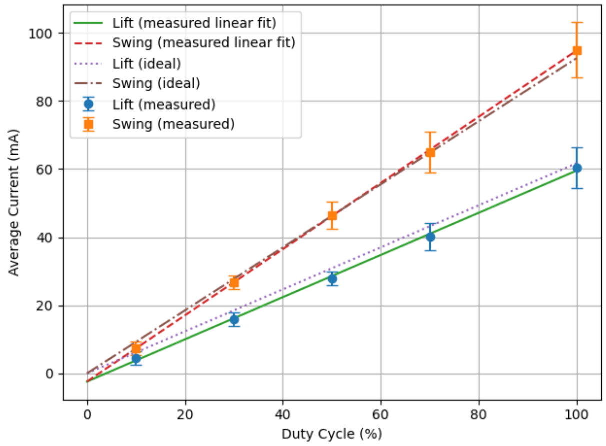

Figure 2: Measured current draw aligns with the ideal PWM model despite expectations of ripple-current losses.

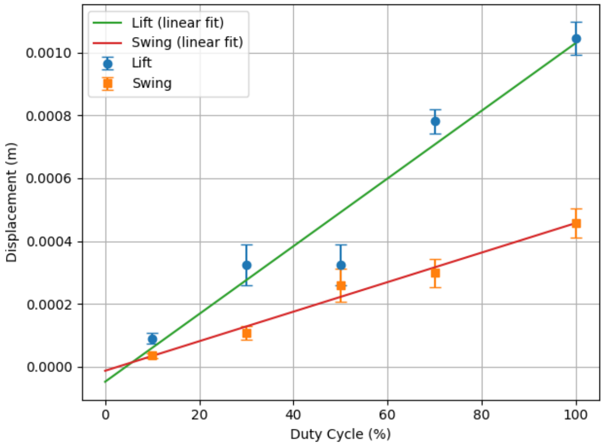

Figure 3: Lift ($R^2 = 0.938$) and swing ($R^2 = 0.987$) VCA displacements collected at $f_d = 50$ Hz are linear in current.

(VEO 710, Phantom) at 2000 frames per second, and processed in Matlab. Displacement was extracted by corner detection using the minimum eigenvalue algorithm [14], implemented within Matlab as the `detectMinEigenFeatures()` function.

We swept input PWM duty cycle at 24 kHz and 3.7 V, and plotted the resulting maximum VCA displacement curves in Figure 3. Displacement of these actuators in the transmission is linear in current with the exception of the measurement at 50% duty. Based on results of subsequent sections, where 50% duty tip displacements agree with overall trends, we consider the data in Figure 3 to be an outlier.

2.4 Thermal Management

At high duty cycles, Joule heating in the actuator coils increases the copper resistance, reducing current draw over time under a fixed applied voltage. Neglecting radiation and assuming a lumped thermal mass, the coil temperature $T(t)$ may be modeled by a first-order energy balance

$$C_{\text{th}} \frac{dT}{dt} = I^2(t)\, R(T) - hA\,(T - T_\infty), \tag{3}$$

where C_{th} is the effective thermal capacitance of the coil and surrounding structure, hA is an effective convective heat transfer coefficient, and T_∞ is ambient temperature.

The temperature dependence of copper resistance is well approximated over the relevant range by

$$R(T) = R_0\big[1 + \alpha\,(T - T_0)\big], \tag{4}$$

where R_0 is the resistance at reference temperature T_0 and $\alpha = 0.393\%$ is the temperature coefficient of resistance for copper.

Under constant applied voltage and fixed duty cycle, this coupled system produces a first-order transient response, in which current decays exponentially toward a steady-state value,

$$I(t) = I_\infty + \big(I_0 - I_\infty\big)\, e^{-t/\tau}, \tag{5}$$

where $\tau = C_{\text{th}}/(hA)$ is the dominant thermal time constant and I_∞ reflects the increased steady-state resistance at elevated temperature.

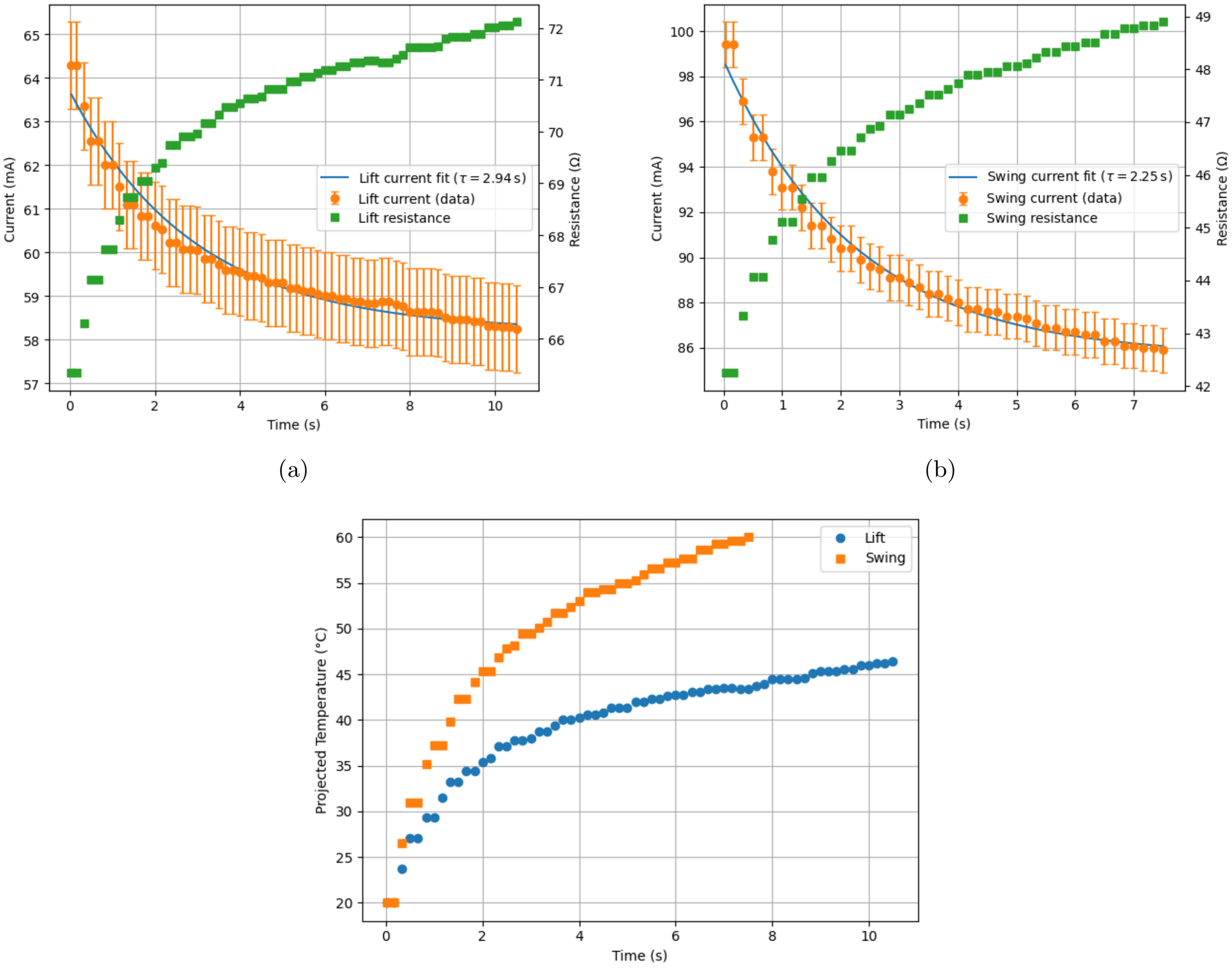

(a)

(b)

(c)

Figure 4: Thermal characterization of VCAs under continuous high-duty operation. (a) Lift and (b) swing actuator current decay and resistance increase at 100% duty show significant temperature effects. (c) Projected actuator temperature based on resistance increase and copper temperature coefficient.

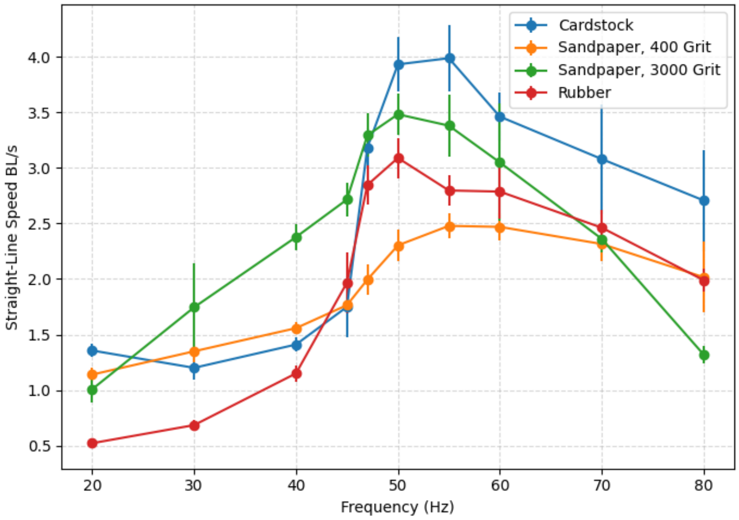

Figure 5: Steady-state straight-line speed of the untethered COMT in a trot indicates a resonant peak at approximately 50 Hz.

We characterized this heating by fitting the exponential current decay observed at peak battery voltage and $D = 100\%$. Due to concerns with actuator wear over long measurement times, we did not record steady-state current draw but instead fit and extrapolated the current curve to estimate the steady-state increase in resistance, as in Figures 4a and 4b.

Taking α as constant throughout our tested temperature range, we projected the steady-state temperature of the lift and swing VCAs at their maximum drive current to be approximately 46.7 °C and 61.1 °C, respectively. The maximum continuous operating temperature of the neodymium magnets (Neodymium 50, M0251, SuperMagnet-Man) surrounding the lift and swing coils is rated at 80 °C [15], and the cyanoacrylate (CA) adhesive (Loctite 495) grounding the leg frame is rated at 120 °C [16]. Based on these values, there should be no long-term issues with the steady-state temperatures we extrapolated.

However, the demonstrated reductions over time in the maximum displacement of both lift and swing actuators is unexplained by this model. As data in Figure 4 was taken only with one of the eight VCAs running at a time, it is possible that significantly higher temperatures are experienced by the actuator assemblies during full gait tests due to the higher power dissipated in the body.

2.5 Straight-Line Speed

We collected high-speed video of the untethered COMT system in a trot, at varied f_d and on four representative surfaces (cardstock, 400-grit sandpaper, 3000-grit sandpaper, and rubber) [17] at 100% duty cycle. The maximum straight-line speed of the system was extracted using the methods in Section 2.3 and displayed in Figure 5. Each dataset was smoothed using a second-order Savitzky–Golay filter to reduce measurement noise, and plotted in Figure 5.

Matlab Simscape Multibody simulations of the transmission linkages using hinge dynamics described in [18] and [19] predicted compliant modes near 130 Hz and 488.7 Hz in the lift and swing linkages, respectively. Ringdown testing pictured in Figure 6 predicted modes near 125 Hz and 250 Hz. However, actuation at any these frequencies proved infeasible in practice due to significant observed ineffective stances (defined as in [11]). The tested frequency range reflected the outer bounds of reliable operation: below 20 Hz and

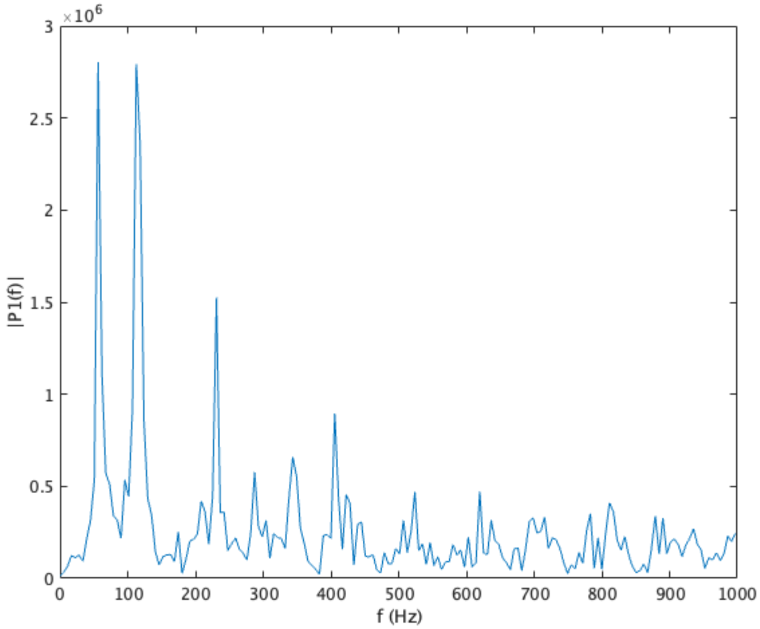

Figure 6: Amplitude spectrum of tip displacement, captured from a 50 Hz square drive at 3.7V, $D = 70\%$.

above 80 Hz, forward motion was not repeatable, reflecting strong variation in stance effectiveness with drive frequency. We attempt to explain the observed peaks in straight-line speed by examining a dynamic model for our transmission system.

2.6 Resonant Effects of Transmission Linkages

In COMT's leg configuration, there are two planar four-bar linkages arranged in series to convert linear motion of the lift and swing actuators into a two-degree-of-freedom (DOF) leg-tip trajectory (Figure 7). Leg-tip motion is described in a local planar frame spanned by the unit vectors $\mathbf{e}_{\parallel}$, oriented parallel to the walking surface, and $\mathbf{e}_{\perp}$, oriented perpendicular to the walking surface. The tip trajectory is then written as

$$\mathbf{x}(t) = x_{\parallel}(t)\,\mathbf{e}_{\parallel} + x_{\perp}(t)\,\mathbf{e}_{\perp}.$$

The leg has a lift transmission ratio (A:B in Figure 1a) of $1:3$, and a swing transmission ratio (C:D in Figure 1b) of $1:2.5$. However, the coupling between lift and swing DOFs in the leg means that the amplified lift and swing displacements do not necessarily occur in $\mathbf{e}_{\perp}$ and $\mathbf{e}_{\parallel}$, respectively. We observe this in Figure 7, where a lift actuation rotates the swing actuator displacement vector counterclockwise.

To quantify this coupling, we construct a transmission geometry matrix

$$A_{\text{geom}} = \begin{bmatrix} \alpha_{\parallel,\text{swing}} & \alpha_{\parallel,\text{lift}} \\ \alpha_{\perp,\text{swing}} & \alpha_{\perp,\text{lift}} \end{bmatrix}, \tag{6}$$

where $\alpha_{i,j}$ can be evaluated by comparing the tip trajectory produced by a set of lift-only and swing-only actuations to VCA displacements recorded at the same time. In an ideal system where lift and swing are fully uncoupled, the matrix would be diagonal, with entries reflecting the scalar transmission ratios of each linkage. In effect, A_{geom} describes the 2-D transmission ratios of each linkage. We can write A_{geom} in terms of measurable quantities as

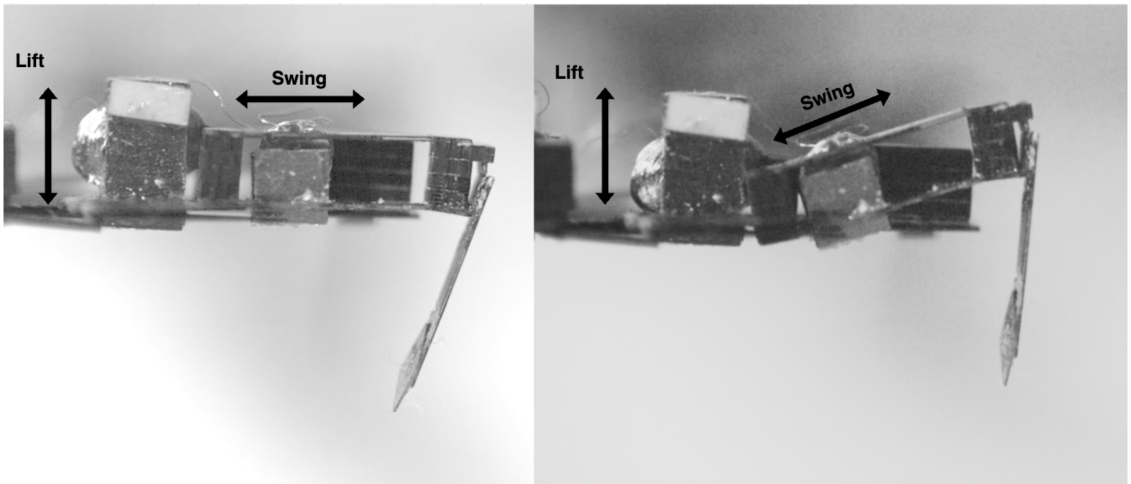

(a) (b)

Figure 7: Lift and swing degrees of freedom are strongly coupled in the series transmission configuration.

$$A_{\text{geom}} = \begin{bmatrix} \dfrac{\Delta x_{\parallel}^{(S)}}{\Delta s_{\text{swing}}} & \dfrac{\Delta x_{\parallel}^{(L)}}{\Delta s_{\text{lift}}} \\ \dfrac{\Delta x_{\perp}^{(S)}}{\Delta s_{\text{swing}}} & \dfrac{\Delta x_{\perp}^{(L)}}{\Delta s_{\text{lift}}} \end{bmatrix}, \tag{7}$$

where Δs_{lift} and Δs_{swing} are the cycle-averaged displacements of the lift and swing VCAs, respectively.

We collected high-speed video of a single series leg under low-frequency ($f_d = 1$ Hz) forcing at the nominal battery voltage of 3.7 V, and varied duty cycle. We processed the data using the methods in Section 2.3. Displacements of each actuator, as well as the leg tip, at a representative duty of 50%, are recorded in Table 2.

Table 2: Leg tip and actuator displacement components used to estimate A_{geom}, measured at 50% duty cycle, $f_d = 1$ Hz.

Actuated DOF	**Direction**	**Tip Displacement** (mm)
Lift	$\mathbf{e}_{\parallel}$	1.27
Lift	$\mathbf{e}_{\perp}$	0.96
Swing	$\mathbf{e}_{\parallel}$	0.524
Swing	$\mathbf{e}_{\perp}$	0.090

DOF	**Actuator Displacement** (mm)
Lift (Actuator)	0.260
Swing (Actuator)	0.323

Substituting the measured values, we can evaluate

$$A_{\text{geom}} = \begin{bmatrix} 2.019 & 3.928 \\ 0.3467 & 2.969 \end{bmatrix}. \tag{8}$$

As expected, A_{geom} describes a significant tip displacement in $\mathbf{e}_{\parallel}$ from lift actuation, which is independent of applied current (Figure 8b) The diagonal entries nominally reflect the scalar transmission ratios

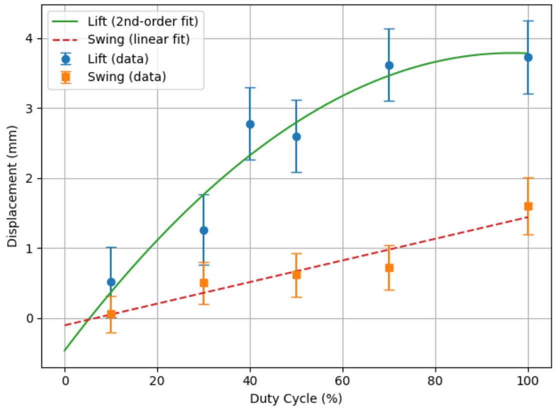

(a)

Duty	**Lift, $\mathbf{e}_\perp$**	**Lift, $\mathbf{e}_\parallel$**	**Swing, $\mathbf{e}_\perp$**	**Swing, $\mathbf{e}_\parallel$**
10%	30.5%	69.5%	22.8%	77.2%
50%	31.2%	68.8%	20.7%	79.3%
100%	36.8%	63.2%	31.4%	68.6%

(b)

Figure 8: Series leg tip displacement.(a) When actuated by lift ($\mathrm{R}^2 = 0.934$) and swing DOFs ($\mathrm{R}^2 = 0.901$) at 50 Hz, tip displacement shows nonlinearities above 70% duty cycle in lift, but is linear across duty cycles in swing. (b) Components of lift and swing actuations in $\mathbf{e}_\parallel$ and $\mathbf{e}_\parallel$ remain relatively constant in current.

of each linkage, but A_{geom} allows us to describe the significant impact of the lift transmission linkage on forward motion, and therefore the necessity of including its dynamics in our evaluation of straight-line speed.

We note that tip displacement induced by the lift actuator saturates above 70% duty cycle (see Figure 8a). This nonlinearity is to be somewhat expected given the nonlinear dynamics associated with the linkage's polyimide flexures outside of their small-angle range [18, 19]. In future work, we will constrain the applied duty cycle to 70%, both to minimize the resistive heating discussed in Section 2.4 and maintain linearity for more predictable control.

Knowing that forward progress is largely determined by actuator tip displacement in $\mathbf{e}_\parallel$, and that both DOFs contribute significantly to this displacement, we can describe the steady-state straight-line speed of COMT as roughly corresponding to the frequency responses of the two transmission linkages. Based on the series transmission architecture, we define

$$G_{\text{leg}}(s) = \frac{\omega_L^2}{s^2 + 2\zeta_L \omega_L s + \omega_L^2} \, \frac{\omega_S^2}{s^2 + 2\zeta_S \omega_S s + \omega_S^2} \tag{9}$$

as the transfer function from a lumped-parameter actuator input to a tip displacement in $\mathbf{e}_\parallel$, with magnitude

$$\left|G_{\text{v}\leftarrow u}(\mathrm{j}\omega)\right| \approx K \frac{\omega_{n1}^2}{\sqrt{(\omega_{n1}^2 - \omega^2)^2 + (2\zeta\,\omega_{n1}\,\omega)^2}} \, \frac{\omega_{n2}^2}{\sqrt{(\omega_{n2}^2 - \omega^2)^2 + (2\zeta\,\omega_{n2}\,\omega)^2}}, \tag{10}$$

where $\omega_{[L,S]}$ and $\zeta_{[L,S]}$ denote the natural frequency and damping ratio of the lift and swing linkages, and K is a scaling constant. We simplify $\zeta_L = \zeta_S = \zeta$ given the mechanical similarity of the two linkages. Additionally, we lump the derivative term $s = j\omega$ into the scaling constant, noting that the frequency-dependent effects of observed ineffective stances largely negate any velocity gains from faster drive frequencies.

2.7 Analysis of Open-Loop Straight-Line Speed

We analyze straight-line speed data in context of the transmission model introduced in Section 2.6. Measured speed data were fit to both the two-mode transmission model and a simpler single-mode second-order magnitude model to ensure that the two-mode model did not overfit measurements. Fit quality was evaluated

Surface & Model	**RMSE**	$\mathbf{R^2}$	**AIC**	**BIC**
Cardstock				
1-mode	0.6177	0.642	-3.64	-2.73
2-mode pure series	0.4343	0.8232	-8.68	-7.47
2-mode with parallel body mode	0.4325	0.8247	-6.77	-5.25
Sandpaper, 400 Grit				
1-mode	0.1457	0.8948	-32.53	-31.62
2-mode pure series	0.0888	0.9609	-40.43	-39.22
2-mode with parallel body mode	0.0888	0.9609	-38.43	-36.91
Sandpaper, 3000 Grit				
1-mode	0.2531	0.9076	-21.48	-20.57
2-mode pure series	0.1274	0.9766	-33.20	-31.99
2-mode with parallel body mode	0.1168	0.9803	-32.94	-31.43
Rubber				
1-mode	0.5257	0.6545	-6.86	-5.95
2-mode pure series	0.3305	0.8635	-14.15	-12.93
2-mode with parallel body mode	0.3305	0.8635	-12.15	-10.63

Table 3: Performance of our system-level model in straight-line speed tests.

using root mean squared error (RMSE), (R^2), and the Akaike and Bayesian Information Criteria (AIC and BIC), which balance model fit with parameter complexity.

Across all four surfaces, the two-mode series transmission model consistently outperformed the single-mode model as displayed in Table 3. RMSE was reduced by 30–50% and AIC/BIC decreased despite penalizing the additional parameter. This pattern indicates that straight-line speed is well described by two dominant resonance modes, consistent with structure of the transmission model. The anomalous system response on 400-grit sandpaper is likely influenced by surface granularity, as the average particle size (23 µm) approaches COMT's nominal swing displacement (100 µm), interfering with leg motion and reducing overall speed.

We note that the frequencies of the resonances observed in this drive frequency range do not correspond to those of the modes predicted by multibody simulations of the transmission linkages (130 Hz, 488.7 Hz) or observed in the tip displacement amplitude spectrum in Figure 6 (125 Hz, 230 Hz). Ground interaction appears to either significantly shift these peaks left or excite other unmodeled resonances in the body.

In addition to the two dominant resonances observed near $f_d \approx 53$ Hz and $f_d \approx 85$ Hz, multiple raw datasets exhibit a secondary peak near $f_d \approx 30$ Hz. This feature is consistent with prior Simscape Multibody simulations predicting a low-frequency body mode at 31 Hz, and therefore cannot be dismissed as measurement noise.

To investigate the body mode's influence, we attempted to extend the transmission model by introducing an additional second-order body mode in parallel with the transmission dynamics (Fig. 10). This augmented model fit the data with lower RMSE and higher R^2 across all surfaces. However, both AIC and BIC increased, indicating that the improved fit does not generalize well beyond the measured data. In future work, we will apply the same experimental framework to an alternative leg configuration of COMT, where DOFs are significantly less coupled, and evaluate whether a comparable two-mode fit is representative of performance.

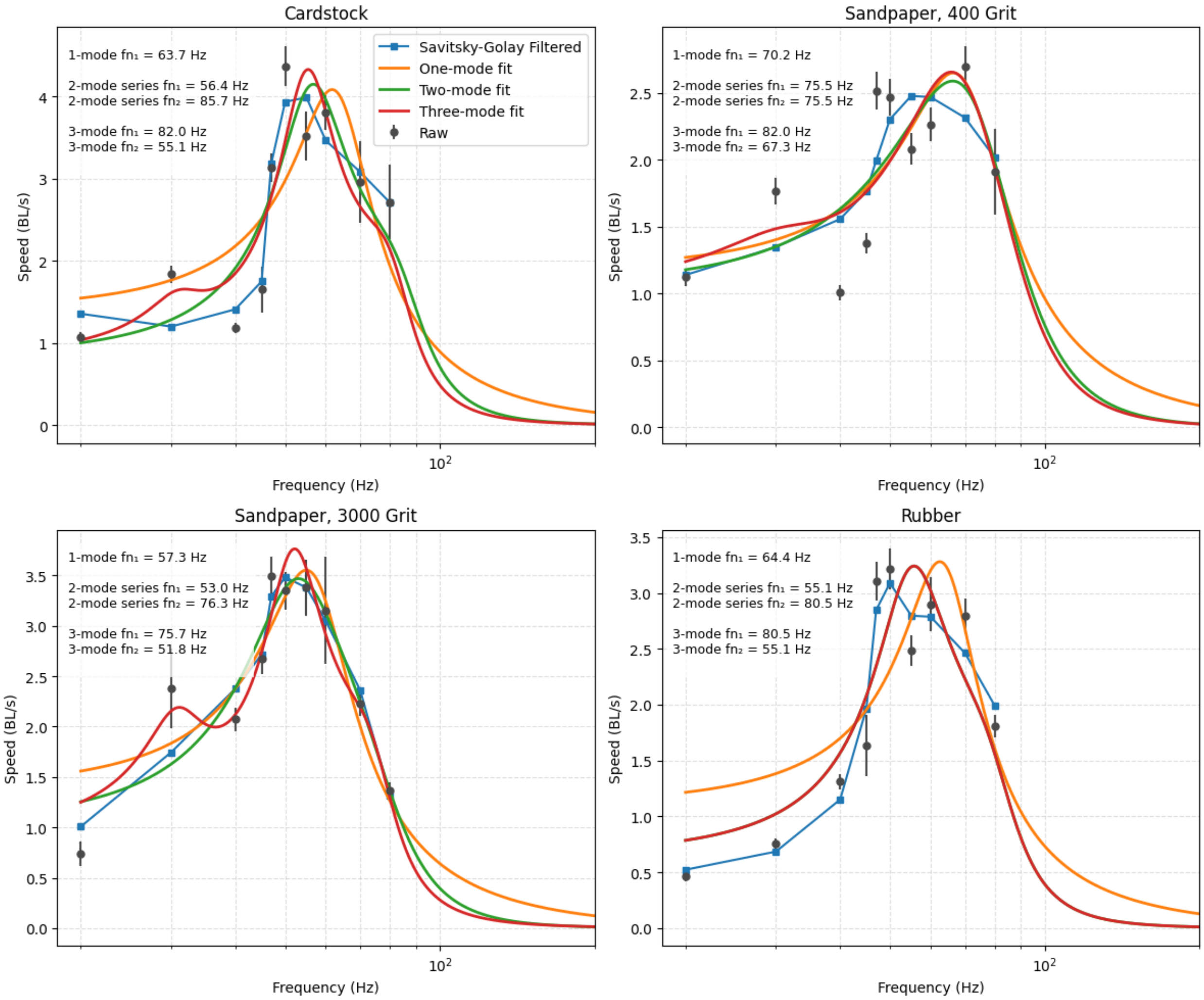

Figure 9: Recorded frequency-speed data reflects two primary resonances. In the two-mode fit, we extract $\zeta = \{0.166,\ 0.340,\ 0.242,\ 0.173\}$ for cardstock, 400-grit sandpaper, 3000-grit sandpaper, and rubber, respectively.

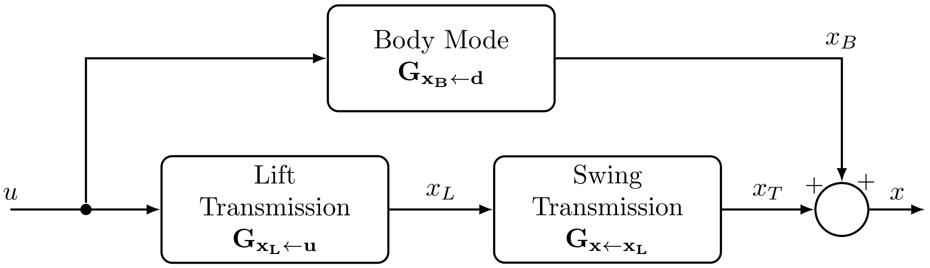

Figure 10: We add an additional parallel mode to the modeled transmission dynamics to capture body resonances.

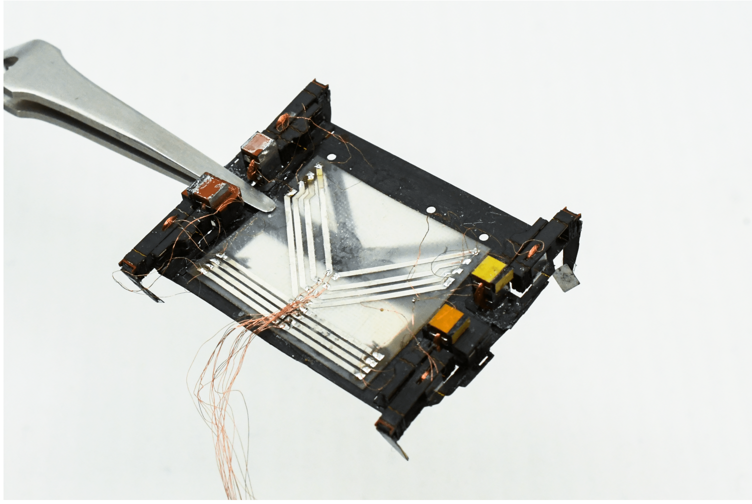

Figure 11: Individual actuators are controlled open-loop with offboard signal generation via a 16-wire tether.

3 Untethered Operation

Realizing the control strategy discussed in Section 2.2 on a severely SWaP-constrained microrobot requires that they be implemented within the compute and power limitations imposed by onboard electronics. To bridge the gap between control design and physical implementation, we describe the custom printed circuit board (PCB) developed to support closed-loop control on COMT.

3.1 Component Selection

COMT's VCAs were previously driven with DC signal input by leveraging multiple dual H-bridge DC motor drivers (DRV8833, Texas Instruments). Independent actuation of all 8 DOFs was possible in a tethered configuration with four external motor drivers (Figure 11), while two motor drivers on the untethered PCB required electrical coupling of diagonal legs (Figure 12). This coupling requirement diminished phase control effectiveness, motivating a board which enables untethered, individual actuator control.

We introduce a subsequent flexible printed circuit (FPC) design, mounted on 25 µm polyimide dielectric. This construction not only reduces weight compared to traditional rigid FR-4 laminate, but also mitigates the impact of the PCB on the resonance of a mechanically-tuned chassis. This PCB, displayed in Figure 13, not only increases the number of DRV8833 drivers to four, but includes a more robust inertial measurement unit (IMU, ICM-20948, Invensense) and a time-of-flight (TOF, VL53L1X, STMicroelectronics) sensor for absolute distance sensing and eventual localization and mapping. Additionally, the new board enables integrated tethered closed-loop experiments with additional test points, allowing real-time evaluation of future state estimation and control strategies.

The microcontroller (MCU) selected (Kinetis MKL46Z256-VLL4, Freescale Semiconductors) was largely a product of previous PCB iterations, maintained for ease of integration with existing software. However, the low-power modes, direct memory access (DMA), and high clock speed available on the KL46 all benefit the speed and power efficiency of our control system.

The IMU selected was specified for 9-DOF operation, low power, and internal sensor fusion, making

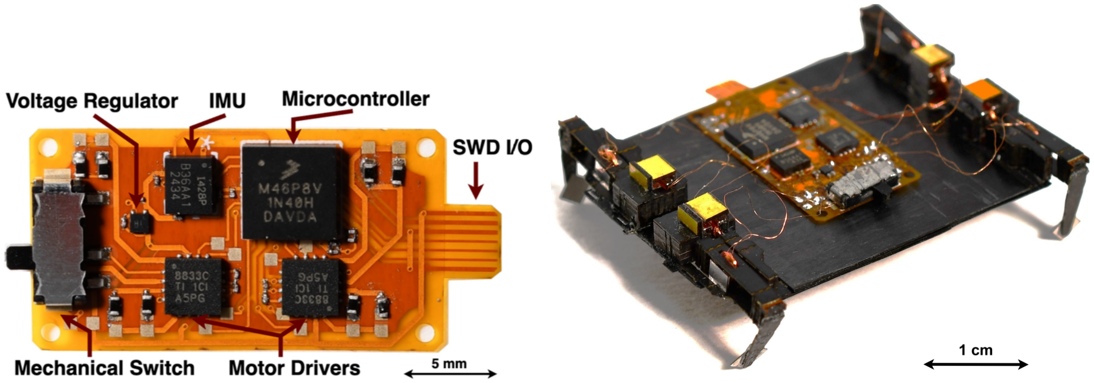

(a) The two-driver PCB.

(b) The fully-assembled system.

Figure 12: The previous untethered COMT with series transmission requiring electrically-coupled DOFs. For untethered operation, the battery is mounted below the chassis pictured.

it ideal for this use case. We compare this to the 6-DOF IMU (ICM-42688, Invensense) deployed on the previous PCB. The resonant effects described in Section 2.6 as a result of periodic actuation contribute to significant low-frequency noise in the accelerometer and gyroscope components of the IMU. The magnetometer, a measure of absolute orientation included in 9-DOF IMUs, is significantly less susceptible to the noise induced by these pulses, and therefore useful for sensor fusion.

However, the Digital Motion Processor (DMP) functionality of the ICM-20948, which allows for internal sensor fusion, was gated by proprietary commercial software from Invensense. Open-source methods to enable the DMP were attempted and failed. An open-source sensor fusion library (Sensor Fusion SDK 7.2, NXP) for Kinetis Microcontrollers was therefore used to estimate the system absolute orientation from accelerometer, gyroscope, and magnetometer data.

The TOF sensor was selected to provide compact absolute range measurements compatible with the SWaP constraints of the COMT platform. Its small footprint, low integration overhead due to provided libraries, and configurable update rate make it well suited for closed-loop sensing, complementing previous components.

Additional relevant component selection decisions include:

- A lightweight button (NanoT100AS, C&K Switches), latched by a series of discrete N-channel MOSFETs, greatly reduces the weight of the power switching system.
- Additional test points allow for exteral I^2C bus reads and tethered actuation without repeated removal and replacement of the PCB, enabling more robust securing of the board to the robot chassis.

3.2 PCB Design Considerations

Bending and Flexibility

To accommodate the additional components and external interfaces, the PCB is bent about COMT's front face as in Figure 13(b). This not only permits a smaller frame, but creates the mechanism pointing the TOF sensor forward, improving weight and reducing mechanical complexity. However, bending stresses become a

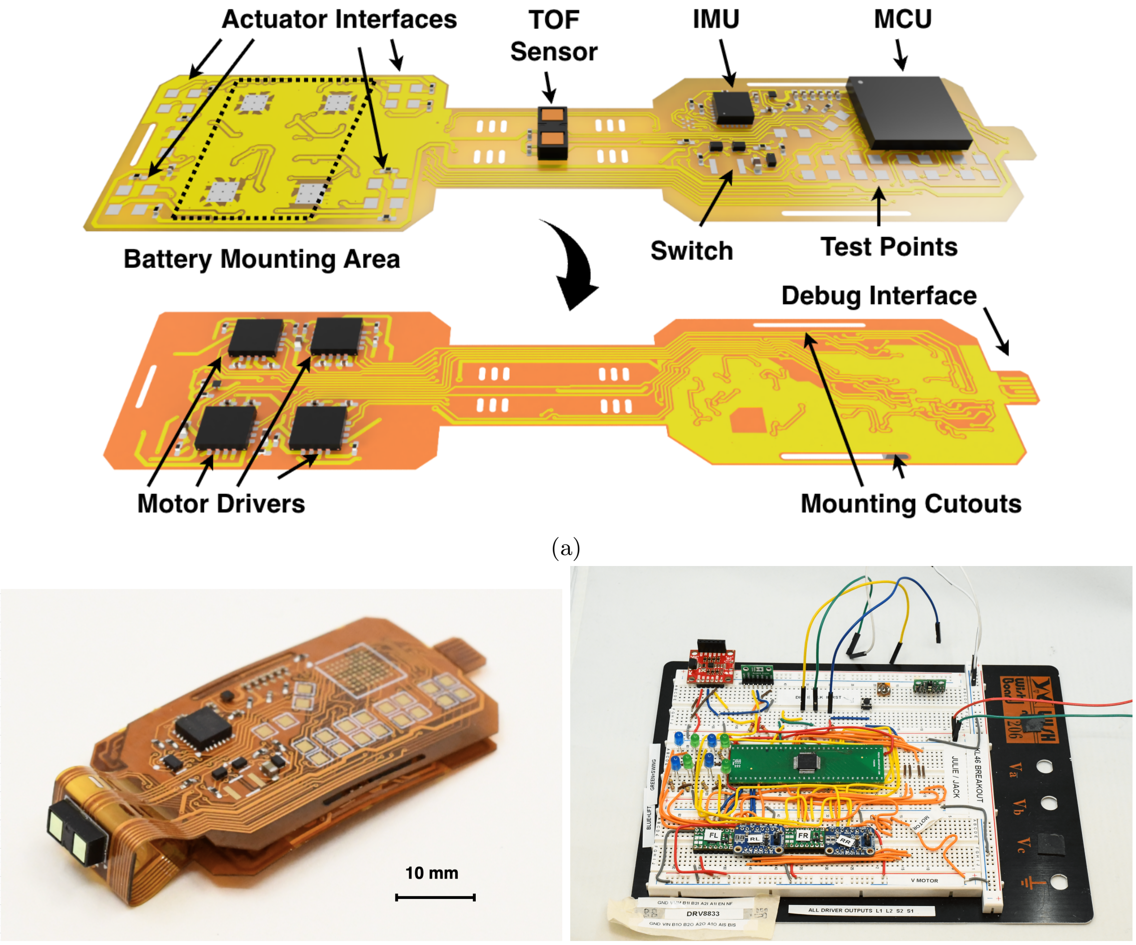

(a)

(b)

(c)

Figure 13: The new COMT PCB, implementing additional sensing, individual actuator control, and integrated tethered testing capability. (a) The outside (top) of the PCB contains the microcontroller, switch, IMU, TOF sensor, test points, and actuator and battery attachment points. The inside (bottom) contains motor drivers and a 'gold finger' connector for external debugging. (b) the PCB is bent about the robot chassis to point the TOF sensor forward and allow for reduced footprint. (c) ICs included in the PCB were evaluated on a breadboard for representative prototyping and tethered operation. (top left) ICM-20948 IMU and VL53L1X TOF sensor. (top center) Serial Wire Debug connectors to an external Segger J-Link debug interface. (center left) status LEDs for each actuator. (center) KL46 microcontroller. (bottom) DRV8833 motor drivers for each DOF.

concern given the small footprint of the board.

We evaluate bending constraints from the manufacturer specification [20]

$$R > 12t$$

for a double-sided board, Where R is the bending radius and t is the thickness of the board. Our stackup (25 µm dielectric, 0.5 oz copper) produces an overall thickness $t = 120$ µm, for a minimum bending radius of

$$R > 1.44 \text{ mm}$$

As evaluated in the configuration in 13(b), no bend falls below $R = 1.5$ mm, placing aggregate bending within the limits of safe operation.

Additional considerations exist to ensure that the PCB remains mechanically stable long-term. The specification [20] recommends staggered trace design over beam traces (see Figure 14) to minimize stress in flexed components, a strategy we employ over the flexed connector on which the TOF sensor is mounted. We also employ cut-outs (see Figure 13a, center) to reduce the force required to secure the PCB in a bent configuration.

Footprint and Mass

The total mass of the PCB is 680 mg. This mass significantly exceeds the design budget of 500 mg specified in Executive Summary Section 2. We attribute this discrepancy primarily to unexpected mass in the polyimide stiffeners placed to reduce deformation under sensitive ICs. In future design iterations, we will investigate modifications to COMT's chassis in order to support these systems without excessive weight. The footprint of the PCB, however, is within the design specifications, and fits on the $\sim$ 20 mm × 15 mm chassis. The inclination of the TOF sensor, as mounted according to Figure 13, is adjustable by varying the mounting position of the top half of the PCB.

Component Placement and Routing

Although it made significant strides toward towards untethered operation of the COMT system and inspired many of the decisions in this work, we nonetheless identified critical performance and reliability issues in the previous PCB (Figure 12a). Specifically, a single shared ground plane for all components caused interference when the actuators were switched on, and excessive length of current-carrying traces, combined with poor ground return, caused significant voltage supply fluctuation to the MCU. Wherever possible, we adhered to the industry standard IPC-2221A [4] for PCB design to mitigate these concerns in our board.

We design and route traces between components based on (a) current-carrying capacity, to mitigate thermal degradation over time, and (b) voltage drop, to mitigate the issues caused by under-supplying onboard ICs. Current sizing is governed by the formula

$$I = k\Delta T^{0.44}(wt)^{0.725} \tag{11}$$

where I is the current in amperes, w and t are the trace width and thickness in mils (1 mm $\approx$ 39.37mil), respectively, ΔT is the temperature rise in °C, and $k = 0.024$ is a constant describing the solder masking present over most traces. We based all trace widths on a rated temperature increase of 20°C and thickness of 35µm, specifying a minimum factor of safety of 1.5 to guard against failure in unexpected loading conditions. In cases where the manufacturer minimum recommended trace width for 0.5 oz copper (0.15 mm including a 1.5 factor of safety) exceeded the minimum calculated current-carrying trace width, we chose the former.

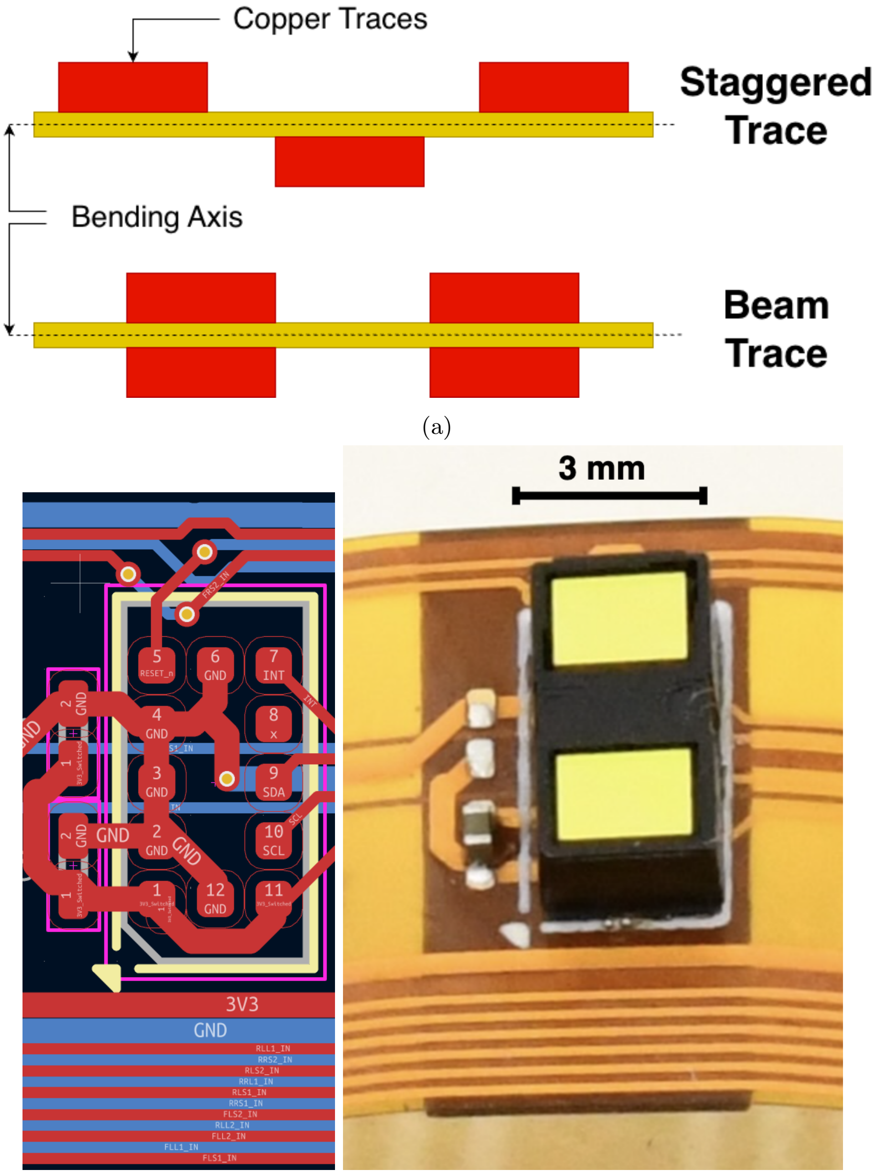

(a)

(b)

(c)

Figure 14: Trace alignment. (a) Staggered traces reduce the effective thickness of bent material compared to beam traces. (b) We implement staggered traces through the bent TOF sensor mount pictured in (c) to ease stresses in the new PCB.

While not necessarily applicable to thermal load or trace voltage drops, the high inductive load of our system relative to its size requires careful consideration of signal decoupling and ground return paths. According to IPC-2221A-06-01 [4], we route a ground trace alongside each of the motor driver signal paths in Figure 14c and 14b. This routing minimizes loop area created by signal return paths, reducing inductive coupling and improving signal integrity. Additionally, we place adequately-sized decoupling capacitors as close to sensitive ICs as possible to decouple their voltage inputs from high-frequency variance in reference potential, according to IPC-2221A Section 6.1.2 [4].

3.3 Onboard Actuator Signal Generation

The limited number of PWM channels (12, separated into three modules) onboard the KL46 mean that a PWM output cannot be assigned to each of the 16 input pins required to independently actuate each of COMT's eight DOFs. To circumvent this constraint, we drive one input channel of the motor driver at a fixed PWM frequency and use the other as a low-frequency GPIO 'gate' to control the direction of the actuator, per Table 4, taking advantage of the shoot-through protection present on the DRV8833.

Table 4: PWM Control of Motor Speed, adapted from [21]

xIN1	xIN2	Function
PWM	0	Forward PWM, fast decay
1	PWM	Forward PWM, slow decay
0	PWM	Reverse PWM, fast decay
PWM	1	Reverse PWM, slow decay

The DRV8833 datasheet specifies that forward and reverse PWM control using only one PWM-capable input is possible, but subject to asymmetrical decay modes between directions. Depending on the polarity of the coil connection, one direction is subject to more ripple current than the other, increasing potential heating loss. The effective duty cycle of the system is determined by the PWM input duty cycle when the gate input is low, as this duty cycle must be inverted when the gate pin flips high to produce the same average current as the ideal, two-PWM input scheme according to Table 4.

We conducted experiments to quantify the impact of decay mode asymmetry on actuator displacements and current draw in the series leg configuration with PWM at 24 kHz. With the robot in tethered configuration (see Figure 12, 13c), actuated a single lift actuator mounted in a series leg (see Figure 1), we observed that downward and rearward displacements of the lift and swing actuators, respectively, were unaffected by polarity. Average current through the lift VCA was also independent of polarity. We measured the current draw of the fast-decay signal to be approximately 4% greater than slow-decay across both actuation directions (Figure 16), an acceptable loss given the significant decrease in system complexity and overall power consumption that the one-pin PWM gating scheme enables.

The gate signal strategy described above produces a square pulse train motor input, requiring minimal duty-cycle switching operations and low computational overhead. However, the sharp transitions inherent to this wave introduce significant high-frequency content according to its Fourier series:

$$u(t) = \frac{4A}{\pi} \sum_{k=1,3,5,\ldots}^{\infty} \frac{1}{k} \sin(2\pi k f_d t)\,, \tag{12}$$

where $u(t)$ is the actuator input voltage, A is the amplitude, T is the period, and f_d is the drive (gate switching) frequency. The third and fifth harmonic of this signal in particular can excite undesirable mechanical resonances in the leg and chassis structures, leading to increased displacement in potentially unproductive directions. However, it is possible that the harmonic content of the 50 Hz square wave as applied to the robot in the straight-line tests in Section 2.7 actually produced the resonant peak observed around 50 Hz. The third and fifth harmonics of the 50 Hz square wave (at 150 and 250 Hz) align closely with the resonances of the lift and swing transmission linkages observed in the tip displacement amplitude spectrum of Figure 6.

We will continue to explore the effect of square drive harmonics on system response in future work. One possible approach to mitigating the adverse resonant effects of the square gate signal is to vary the duty cycle with higher time resolution, smoothing the effective current to approximate a sinusoid and concentrating excitation near a single dominant frequency, as in Figure 15.

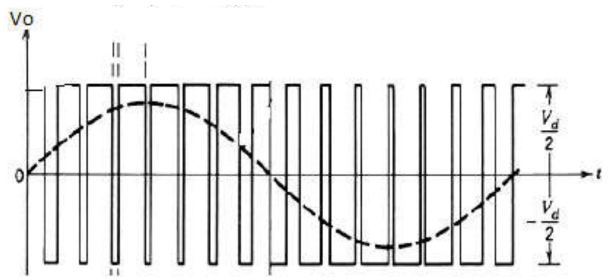

Figure 15: A lower-frequency sinusoid is approximated by varying high-frequency PWM duty cycle (adapted from Aboadla et al. [22]).

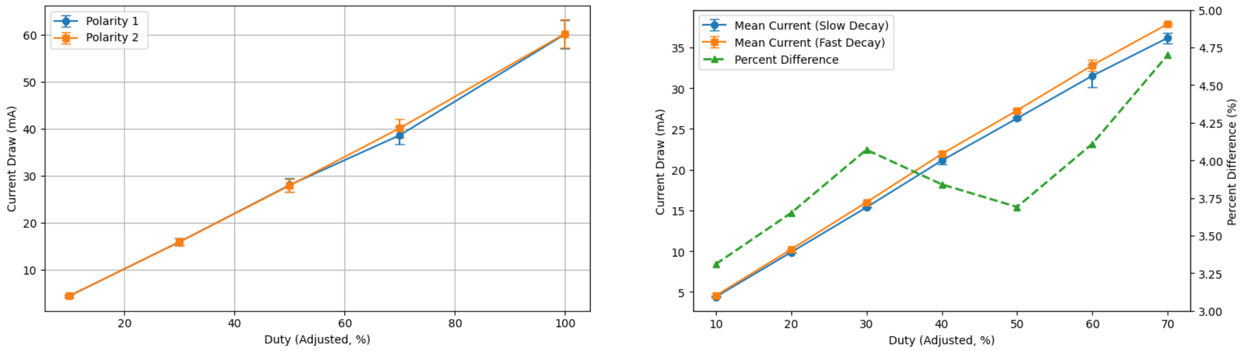

Figure 16: Lift current draw under motor driver PWM decay modes. (a) Polarity 1 corresponds to lift-down actuation in slow-decay mode and lift-up actuation in fast-decay mode, while Polarity 2 reverses this assignment. (b) Current draw is averaged between actuation directions to isolate the effect of each decay mode.

3.4 Closed-Loop Control

The embedded control software is organized as a set of interrupt-driven loops that separate high-frequency actuation timing from lower-frequency closed-loop feedback and sensor acquisition. This structure allows precise enforcement of gait phasing while accommodating the latency and bandwidth limitations of onboard sensing.

At the lowest level, an actuation loop executes on a dedicated periodic interrupt timer (PIT channel 1) at a rate proportional to the selected gait frequency, subdivided into 256 phase slices per gait cycle for

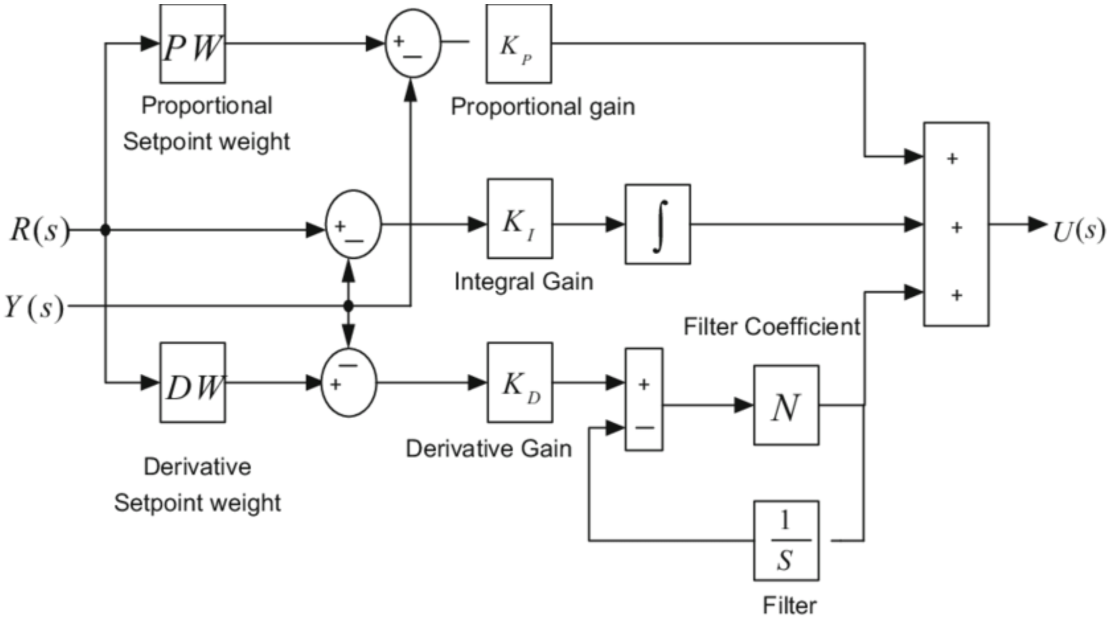

Figure 17: Frequency-domain representation of the two-degree-of-freedom PID controller (Adapted from [23]). For both position and orientation control loops, $R(s)$ and $Y(s)$ define the reference and output states, respectively. We vary actuator current based on the weighted sum of control inputs $U(s)$ from each loop.

8-bit phase resolution. On each tick, the actuation handler advances through a precomputed gait phasing calendar and updates the corresponding timer/PWM (TPM) duty cycles and GPIO states, ensuring that all eight actuator coils execute their scheduled up–down transitions with deterministic timing. This sequence is open-loop in phase, with inter- and intra-leg phasing fixed by the selected gait, but it directly realizes the instantaneous duty-cycle commands supplied by higher-level controllers. As such, it serves as the inner execution loop that translates duty-cycle requests into synchronized physical actuation.

Closed-loop control is implemented in a supervisory control loop running at a rate proportional to the gait frequency, on a second periodic interrupt timer (PIT channel 0). At each iteration, this loop takes in the most recent process variables (range measurements from the TOF sensor and body heading estimates from the IMU) and processes them through two 2-DOF Q16.16 fixed-point proportional–integral–derivative (PID) controllers, according to Figure 17. A distance controller regulates body position, while a yaw controller regulates heading. We use fixed-point math to ease timing constraints, as floating-point operations in our MCU (which is not equipped with a floating point unit) could prove to be a timing bottleneck in the future. The outputs of these controllers are combined into a per-leg duty-cycle command, which is passed to the actuation layer so that subsequent actuation ticks reflect the corrected control inputs. In this way, trajectory feedback is closed on the order of a few milliseconds, while actuator timing remains active at much higher rates.

The 2-DOF PID controller allows for decoupling of setpoint tracking and disturbance rejection. This separation is particularly advantageous in systems where aggressive setpoint tracking would otherwise excite resonant dynamics or amplify noise [24], especially useful given the many flexural modes of the COMT chassis and legs. As a result, we expect to achieve faster, better-damped responses with reduced overshoot while maintaining stability margins comparable to or better than conventional PID control.

Sensor acquisition is handled by asynchronous state machines operating beneath the control layer. The TOF sensor is serviced via an interrupt-driven I^{2}C handler that triggers immediately upon measurement completion and stages the result for the next control update. In parallel, IMU data is acquired using a GPIO interrupt to initiate a separate I^{2}C state machine tailored to the ICM-20948's FIFO buffer, allowing gyro, accelerometer, and eventually DMP data to be streamed without stalling the processor. These mechanisms ensure that each control cycle operates on updated sensor data while preserving real-time guarantees for actuator timing.

To accommodate the slow refresh rate (≤ 60 Hz) of the TOF sensor and blocking I^{2}C operations required by its proprietary drivers, we pass output range updates through a Q16.16 fixed-point Kalman filter running at the prescribed control loop frequency. Currently, this filter operates with simple first-order decay in velocity, according to the state-space dynamics

$$A = \begin{bmatrix} 0 & 1 \\ 0 & -d/m \end{bmatrix} \; B = \begin{bmatrix} 0 \\ 1/m \end{bmatrix} \; q = \begin{bmatrix} x \\ \dot{x} \end{bmatrix}. \tag{13}$$

where d and m are lumped-parameter terms which roughly correspond to drag and inertia, respectively, and x is absolute position. We will derive these terms, as well as the Kalman process noise covariance Σ_z and sensor noise covariance Σ_u, from open-loop identification of the assembled COMT system. More robust time-domain system identification to expand on the model introduced in Section 2.7 will likely prove useful in improving this filter's predictive accuracy.

4 Discussion

In this work, we iterate on the trajectory control strategy of the COMT platform. Moving away from exclusively phase-based control, which has proven difficult to tune reliably in our system, we implement current-controlled differential drive, leveraging built-in features of COTS drivers to overcome MCU output channel limitations. These advances are enabled in large part by the new custom PCB developed in this work. By integrating high-rate PWM current control, inertial sensing, and time-of-flight ranging into a compact, lightweight electronics and software stack, we provide the hardware foundation required to exploit resonance-aware trajectory control strategies in an untethered platform.

Iteration on the low-level control software, especially in implementing quasi-sinusoidal PWM, will likely be necessary for more reliable control of the system. Additionally, we will work towards a more reliable open-loop turning strategy to mitigate the inconsistencies inherent to hand-assembled actuators. Future work will focus on the closed-loop performance of the COMT system, enabled by the onboard sensors and controller introduced here.

5 Acknowledgements

This work would not have been possible without Julie Villamil, whose ongoing support as the primary contributor to the COMT robot is invaluable. Additionally, I would like to thank: Nicole Li, for her previous COMT PCB design; Harry Gao, for additional PCB design and component selection guidance; Cameron Urban, for assistance with multi-body simulations; Lucca Correia, for assistance with data analysis software; and Professor Farrell Helbling, principal investigator, for the research opportunity and laboratory resources. This work was funded in large part by the Cornell Engineering Office of Inclusive Excellence (OIE) Fall 2025 Undergraduate Research Grant.

References

[1] N. Doshi, K. Jayaram, B. Goldberg, and R. J. Wood, "Phase control for a legged microrobot operating at resonance," in *2017 IEEE International Conference on Robotics and Automation (ICRA)*, 2017, pp. 5969–5975.

[2] B. Goldberg, N. Doshi, and R. J. Wood, "High speed trajectory control using an experimental maneuverability model for an insect-scale legged robot," in *Proceedings of the 2017 IEEE International Conference on Robotics and Automation (ICRA)*, Singapore, 2017, pp. 3538–3545.

[3] O. Ozcan, A. T. Baisch, and R. J. Wood, "Design and feedback control of a biologically-inspired miniature quadruped," in *2013 IEEE/RSJ International Conference on Intelligent Robots and Systems (IROS)*. Tokyo, Japan: IEEE, Nov. 2013, pp. 1438–1444.

[4] IPC, "Ipc-2221a: Generic standard on printed board design," IPC (Association Connecting Electronics Industries), Tech. Rep. IPC-2221A, May 2003, released May 2003.

[5] N. Doshi, B. Goldberg, R. Sahai, N. Jafferis, D. Aukes, and R. J. Wood, "Model-driven design for flexure-based microrobots," in *IEEE/RSJ International Conference on Intelligent Robots and Systems (IROS)*, 2015, pp. 4119–4126.

[6] R. Bruhwiler, B. Goldberg, N. Doshi, O. Ozcan, N. Jafferis, M. Karpelson, and R. J. Wood, "Feedback control of a legged microrobot with on-board sensing," in *Proceedings of the IEEE/RSJ International Conference on Intelligent Robots and Systems (IROS)*. IEEE, 2015, pp. 5727–5733.

[7] D. W. Haldane, K. C. Peterson, F. L. Garcia Bermudez, and R. S. Fearing, "Animal-inspired design and aerodynamic stabilization of a hexapedal millirobot," in *2013 IEEE International Conference on Robotics and Automation (ICRA)*. Karlsruhe, Germany: IEEE, 2013, pp. 3279–3286.

[8] Z. Liu, W. Zhan, X. Liu, Y. Zhu, M. Qi, J. Leng, L. Wei, S. Han, X. Wu, and X. Yan, "A wireless controlled robotic insect with ultrafast untethered running speeds," *Nature Communications*, vol. 15, no. 3815, 2024. [Online]. Available: https://doi.org/10.1038/s41467-024-47812-5

[9] J. P. Whitney, P. S. Sreetharan, K. Y. Ma, and R. J. Wood, "Pop-up book mems," *Journal of Micromechanics and Microengineering*, vol. 21, no. 11, p. 115021, 2011.

[10] Y. Fukuoka, Y. Habu, and T. Fukui, "A simple rule for quadrupedal gait generation determined by leg loading feedback: a modeling study," *Scientific Reports*, vol. 5, p. 8169, 2015.

[11] B. Goldberg, N. Doshi, K. Jayaram, J.-S. Koh, and R. J. Wood, "A high-speed motion capture method and performance metrics for studying gaits on an insect-scale legged robot," in *IEEE/RSJ International Conference on Intelligent Robots and Systems (IROS)*, 2017, pp. 3964–3970.

[12] R. J. Sandor, "Pwm motor control: Model and servo analysis," Master's thesis, Rochester Institute of Technology, 1984. [Online]. Available: https://repository.rit.edu/cgi/viewcontent.cgi?article=6644&context=theses

[13] W. M. J. Leach, "Loudspeaker voice-coil inductance losses: Circuit models, parameter estimation, and effect on frequency response," *Journal of the Audio Engineering Society*, vol. 50, no. 6, pp. 442–449, Jun. 2002.

[14] J. Shi and C. Tomasi, "Good features to track," in *Proceedings of the IEEE Conference on Computer Vision and Pattern Recognition*, Jun. 1994, pp. 593–600.

[15] supermagnete.de. (n.d.) Magnetic grade (temperature resistance: N up to 80 °c). States the grade convention that magnets with letter N can be used up to 80 °C (maximum operating temperature). [Online]. Available: https://www.supermagnete.de/eng/magnetism/Grade

[16] Henkel Adhesives. (n.d.) Loctite® 495 — product page (operating temperature: -40 to 120 °c). Lists operating temperature range of LOCTITE 495 as -40 to 120 °C. [Online]. Available: https://www.henkel-adhesives.com/id/en/product/instant-adhesives/loctite_4950.html

[17] N. Doshi, K. O. Goldberg, K. Jayaram, and R. J. Wood, "Contact-implicit optimization for dynamic locomotion on compliant robots," in *Proceedings of Robotics: Science and Systems (RSS)*, 2019.

[18] R. Malka, A. L. Desbiens, Y. Chen, and R. J. Wood, "Principles of microscale flexure hinge design for enhanced endurance," in *IEEE/RSJ International Conference on Intelligent Robots and Systems (IROS)*, 2014, pp. 2879–2885.

[19] M. Goldfarb and J. E. Speich, "A well-behaved revolute flexure joint for compliant mechanism design," *Journal of Mechanical Design*, vol. 121, no. 3, pp. 424–429, 1999.

[20] JLCPCB. Flex pcb designing useful tips. [Online]. Available: https://jlcpcb.com/blog/flex-pcb-designing-useful-tips---jlcpcb

[21] T. Instruments. (2024) DRV8833 dual h-bridge motor driver datasheet. https://www.ti.com/lit/ds/symlink/drv8833.pdf. Accessed: 2025-12-14.

[22] E. H. E. Aboadla, S. Khan, M. H. Habaebi, T. S. Gunawan, B. A. Hamidah, and M. B. Yaacob, "Effect of modulation index of pulse width modulation inverter on total harmonic distortion for sinusoidal," in *2016 International Conference on Intelligent Systems Engineering (ICISE)*. IEEE, 2016.

[23] N. C. Patel, M. K. Debnath, B. K. Sahu, and P. Das, "2dof-pid controller-based load frequency control of linear/nonlinear unified power system," in *Proceedings of the International Conference on Intelligent Computing and Applications (ICICA) 2018*, 2018, available via ResearchGate. [Online]. Available: https://www.researchgate.net/publication/327545605_2DOF-PID_Controller-Based_Load_Frequency_Control_of_LinearNonlinear_Unified_Power_System_Proceedings_of_ICICA_2018

[24] M. Yukitomo, T. Shigemasa, Y. Baba, and F. Kojima, "A two degrees of freedom pid control system, its features and applications," in *2004 5th Asian Control Conference (IEEE Cat. No.04EX904)*, vol. 1, 2004, pp. 456–459 Vol.1.